Available online at www.CivileJournal.org

Civil Engineering Journal

(E-ISSN: 2476-3055; ISSN: 2676-6957)

Vol. 12, No. 02, February, 2026

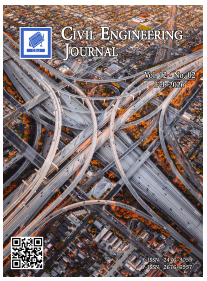

Structural Behavior of Beam-Column Connection Using Post-Installed Steel and GFRP Rebars

Borkan M. Mutashar [1, 2], Oday Asal Salih [1*], Suhaib Y. Kasim [1]

[1] Department of Civil Engineering, College of Engineering, University of Mosul, Mosul 41002, Iraq.

[2] Department of Environmental Technologies, College of Environmental Sciences, University of Mosul, Mosul 41001, Iraq.

Received 14 November 2025; Revised 22 January 2026; Accepted 27 January 2026; Published 01 February 2026

Abstract

This study investigates the performance of steel and GFRP bars as post-installed reinforcement for retrofitting concrete infrastructure through experimental evaluation of the structural performance of the beam-column connection specimens. Three groups of concrete specimens were tested under flexural loading to investigate the influence of bar diameter, bar material (Steel vs. GFRP), and installation method on failure modes, load-deflection curves, and bond strength. The main failure mode at the connections was concrete breakout; however, specimens reinforced with small-diameter post-installed bars tended to fail by bar pullout. The load capacity increases by 9.64% and 12.5% when the diameter of the post-installed GFRP bar increases from 12 to 16 mm and 20 mm, respectively, and the deflection at the midspan of the beam decreases by 17.9% and 33.6% for 16 and 20 mm bars. Specimens with cast-installed reinforcements showed comparable load capacity to post-installed specimens but exhibited lower displacements. Increasing bar diameter reduced bond strength, and GFRP bars showed lower bond strength than steel bars. Overall, the results highlight the potential of GFRP bars as reliable post-installed reinforcement for strengthening critical concrete connections.

Keywords: Post-Installed Bars; GFRP Bars; Beam-Column Connection; Bond Behavior; Adhesive Anchorage; Self-Consolidating Concrete.

1. Introduction

Post-installed reinforcing (PIR) bars, used as adhesive anchors, are among the most prevalent anchoring solutions for retrofitting older structures and strengthening newly cast structural members [1]. PIR bars can be effectively utilized in any region of hardened concrete for rehabilitation and strengthening initiatives, including floor slab connections, wall and beam connections, beam and column connections, vertical connections, and major structural repairs. Moreover, incorporating PIR in beam-column connections enhances their vital role in RC frames [2-4].

The main method of load transfer between concrete and reinforcement (including GFRP) comprises chemical adhesion, mechanical anchoring between the concrete and reinforcement bars, and frictional resistance. The relative contribution of mechanisms evolves as the concrete member ages, where the chemical bond between concrete and reinforcement weakens throughout its lifespan [5-7]. The adhesive anchors rely on the bond between the reinforcement and the bonding agent, or the bonding agent itself, along the concrete, to transmit stresses [8].

Post-installation is a sustainable approach that minimizes operational costs, environmental effects, and resource consumption [9]. PIR techniques have acquired a significant role in retrofitting and restoring aged infrastructure [10]. Cook et al. (1998) demonstrated the sensitivity of PIR systems to drilling conditions and environmental parameters, including temperature and humidity, thereby establishing a fundamental comprehension of their intricate behavior [11].

* Corresponding author: odaycivileng@uomosul.edu.iq

https://doi.org/10.28991/CEJ-2026-012-02-08

Since the invention of epoxy-based adhesives in the 1990s, cementitious adhesives have gradually been replaced by chemical-based adhesive PIR systems. Steel bars used as PIR with proper chemical adhesive binders exhibited comparable or higher bonding capacity than cast-in straight bars, especially when using shorter embedment lengths [12]. This performance is significantly influenced by the compatibility of adhesive stiffness with the mechanical properties of the bars [13]. Although some PIR systems have bond strengths that are remarkably higher than those of cast-in rebar, they are only regarded as being equal to cast-in rebar at most, due to existing design standards; the utilization of the higher measured capacity is not approved [14-16].

Mahrenholtz et al. (2015) emphasized discrepancies in the design of PIR systems as bonded anchors and cast-in reinforcement, revealing substantial variations in design assumptions and permissible bond stresses [17]. Agarwal [18] also demonstrates a key difference in the load transmission process between cast-in rebars and post-installed rebars, which vary because of the existence of an extra coating layer of the adhesive material separating the rebar from the concrete. In a cast-in approach where reinforcement is incorporated inside concrete under the influence of tension, the axial force propagates across the length of the rebar, inducing circumferential compressive stresses via the ribs towards the adjacent concrete. The resulting stresses may lead the adjacent concrete to burst. Conversely, in the post-installed system, failure may arise at the two interfaces of rebar/adhesive or adhesive/concrete; nevertheless, this supplementary layer of adhesive beneficially influences the system by redistributing radial pressure from the ribs to the adjacent concrete.

Many investigations have been conducted on the performance of PIR. However, most previous research has primarily focused on the pull-out capacities of steel rebars as PIR using small-scale specimens, which do not replicate the stress conditions in structural members [19, 20]. Despite the increasing applicability of PIR systems, no published research has been conducted to assess the performance of GFRP bars used as PIR in beam-column connections. Due to the growing impact of climate change on RC infrastructures, GFRP rebars have been introduced as an alternative to steel reinforcement for structures vulnerable to harsh environmental conditions [21, 22]. Mahrenholtz (2012) reported that standard anchor testing procedures tend to overlook complex failure modes, such as concrete breakout and bond deterioration under structural loads [23].

This study investigates the structural and anchorage behavior of reinforced concrete beam-column connections incorporating post-installed steel and GFRP bars. The experimental program examines the effects of bar diameter, material, and installation method on crack patterns, failure mode, flexural performance, and bond performance of PIR under monotonic loading. Cracked-section analysis was used to calculate bond stresses, and the results were compared in terms of failure mechanisms, load-displacement relationships, bond stresses, and strain measurements to understand how bar diameter, bar material, and installation method influence system behavior.

Most previous research concentrated solely on the pull-out capacity of GFRP bars as PIR embedded in small specimens. Therefore, the present work provides a deeper understanding of the anchorage performance of GFRP bars used as PIR in more realistic experimental models of beam-column connections subjected to flexural loading. The investigation included bar material (GFRP and Steel), bar size, and installation method on full-scale beam-column connection specimens. The failure mode, bond strength, and load-displacement results were investigated. This research offers a more realistic evaluation of the PIR and contributes to the future guidelines for using GFRP and steel bars as PIR in structural connections.

2. Materials

2.1. Steel and GFRP Bars

For the beams and columns, Deformed steel reinforcing bars were used. The size bars (12 mm and 16 mm) served as the primary reinforcement, while the bars (10 mm) served as transverse reinforcement for the beam and the two similar columns. GFRP bars in three different diameters (12 mm, 16 mm, and 20 mm) were employed to strengthen beams longitudinally. This range of commercially available bar diameters was selected to capture the effect of bar size on the structural behavior. The GFRP rebars were tested following the ACI 440.3R-04 requirements [24]. The steel rebars were tested according to A615/A615M-01b [25]. Table 1 shows the obtained yield stress and ultimate tensile strength values for each steel bar, as well as the ultimate tensile strength values for GFRP bars.

Table 1. Properties of Steel and GFRP Bars

Bar Diameter (mm)	Bar Material	Yield Stress (MPa)	Ultimate Stress (MPa)	Elongation
10	Steel	469	653	19.1%
12	Steel	463	696	17.2%
12	GFRP	-	1020	1.3%
16	GFRP	-	913	0.9%
20	GFRP	-	970	1%

2.2. Cement

Locally available Portland cement that complied with ASTM C150 [26] was utilized; Table 2 illustrates the properties of cement.

Table 2. Physical and Chemical Properties of the Cement

No.	Physical Characteristics	Value	Limits % [26]
1	Standard Consistency (w/c)	0.295	
2	Initial setting	120 Minutes	≥45 Minutes
3	Final setting	285 Minutes	≤375 Minutes
4	Compressive strength (3 days)	25.1 MPa	≥12 MPa
5	Compressive strength (7 days)	35.6 MPa	≥19 MPa
6	Fineness (sieve no. 170)	1.8%	≤10
	Chemical composition	**Content %**	**Limits % [26]**
7	SiO_2	21.3	---
8	AL_2O_3	4.8	---
9	Fe_2O_3	5.64	---
10	CaO	59.45	---
11	MgO	2.50	≤6
12	SO_3	2.04	≤3
13	Free Lime	0.89	---
14	Loss on ignition	1.60	≤3
15	Insoluble residue	0.24	≤0.75
16	Solid Solution	19.69	---

2.3. Limestone Powders

Limestone powders (CaCO3) were utilized as a filler, with the particles passing through screen No. 50 (0.3mm) to enhance stability and flow.

2.4. Water

Portable water was used for mixing and curing.

2.5. Fine and Coarse Aggregates

Natural river sand that complied with ASTM C136/C136M-19 [27], as shown in Table 3, served as fine aggregate. A river-rounded shape gravel with a maximum size of 12.5 mm that complied with ASTM C136/C136M-19 [27], as shown in Table 4, was used as a coarse aggregate. Figures 1 and 2 illustrate the sieve analysis of the fine and coarse aggregate.

Table 3. Grading of Fine Aggregate

Sieve Size (mm)	Passing %	Passing % Limits [27]
4.75	90	90-100
2.36	77	75-100
1.18	69	55-90
0.6	53	35-59
0.3	12	8-30
0.15	4	0-10

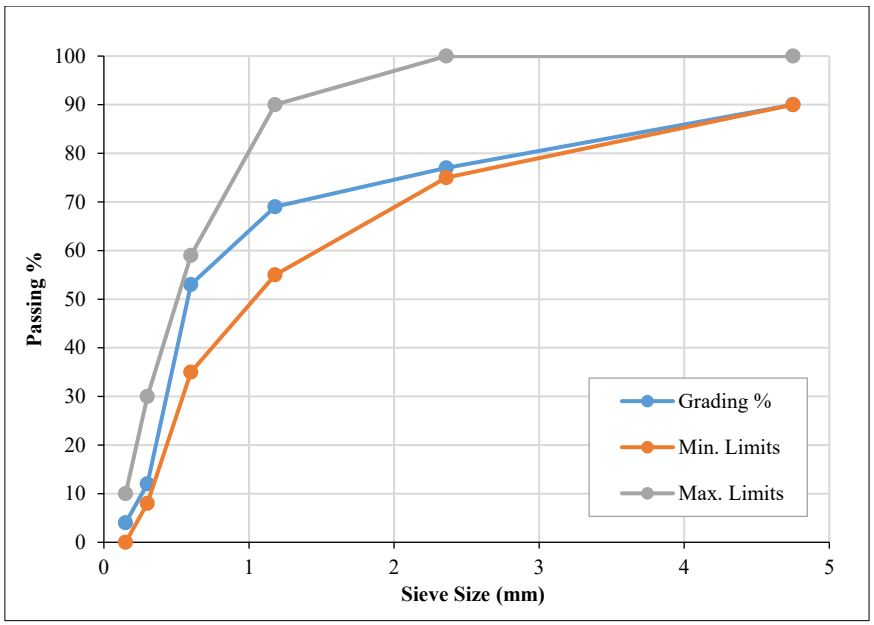

Figure 1. Sieve analysis of fine aggregate

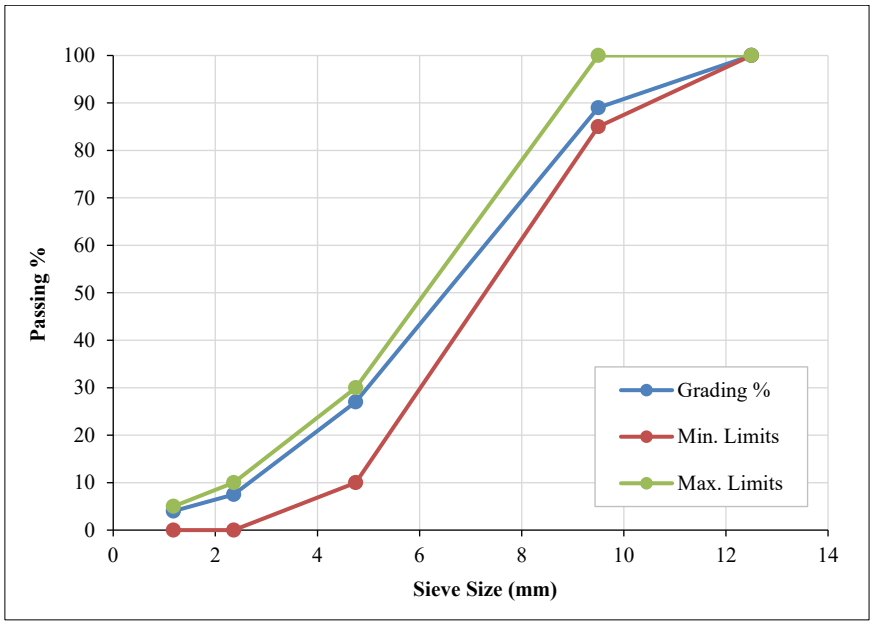

Figure 2. Sieve analysis of coarse aggregate

Table 4. Grading of Coarse Aggregate

Sieve size (mm)	Passing%	Passing % Limits [27]
12.5	100	100
9.5	89	85-100
4.75	27	10-30
2.36	7.5	0-10
1.18	4	0-5

2.6. Hyperplast PC200

Hyperplast PC200 is a highly efficient superplasticizing additive made of polycarboxylic polymers with long chains that are especially designed to allow the quantity of water in the concrete to function more efficiently. This effect may be used in high-strength and flowable concrete mixtures to provide the optimum concrete performance and dependability [28]. Table 5 shows the Hyperplast PC200 Technical Properties at 25°C.

Table 5. Technical Properties of Hyperplast PC200 at 25 °C

Parameter	Specifications [29]
Color	Light yellow liquid
Freezing point	≈ -3°C
Specific gravity	1.05 ± 0.02
Air entrainment	Typically, less than 2% additional air is entrained above the control mix at normal dosages

2.7. Adhesive

For the post-installation of the GFRP reinforcement bars in the embedded region of the columns, Sika Anchor-3030 was used as an adhesive. As specified by the producer (Sika), the mechanical and curing properties are illustrated in Table 6.

Table 6. The mechanical and curing properties of Sika Anchor 3030 [30]

Property		Value
Type		Two-component epoxy adhesive
Color		Grey
Application Temperature		+5 °C to +40 °C
Gel Time (at 20 °C)		25 minutes
Full curing time (at 20 °C)		12 hours
Service Temperature	Long term	-40 °C min. / +50 °C max.
	Short-term	+70 °C
Compressive strength		95 MPa (7 days, +20°C)
Tensile Strength in Flexure		45 MPa (7 days, +20°C)
Tensile Strength		23 MPa (7 days, +20°C)
Modulus of Elasticity in Tension		5500 MPa (7 days, +20°C)

3. Mix Proportions

A self-consolidating concrete (SCC) mix was utilized to ensure sufficient flowability and appropriate infill surrounding the bars that were post-installed. The mix was designed to achieve a compressive strength of 35 MPa at 28 days. The mix was proportioned to 193 kg/m^3 of cement, 37.5 kg/m^3 of limestone powder, 975 kg/m^3 of fine aggregate, 780 kg/m^3 of coarse aggregate, and 1.2% superplasticizer. A water-to-cement ratio of 0.48 was selected. To make sure that the SCC mix complies with the EFNARC's regulations [31]. The three common workability tests were the slump flow and the T50 time tests for indicating flow spread and viscosity (Figure 3), the V-Funnel test for assessing flow time and potential blockage, and the L-Box Test for evaluating passing ability and segregation resistance.

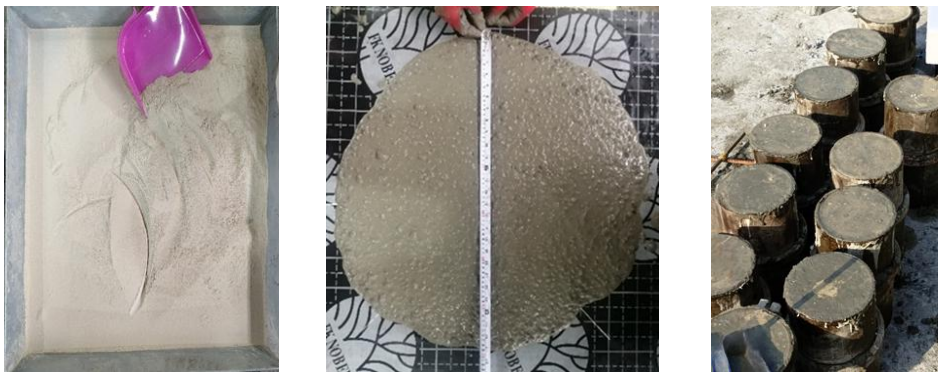

(a) Limestone Powder **(b) Slump Flow Measuring** **(c) Cylinder Casting**

Figure 3. Limestone powder, slump flow measuring, and cylinder casting

The selected SCC had a T50 of 2.4 sec., a V-funnel time of 8 seconds, an L-box ratio of 0.92, and a slump flow diameter of 790 mm, which satisfy the EFNARC's regulations for SCC [31]. A total of twelve standard cylinders of (150 x 300 mm) were cast and cured according to the procedure described in ASTM C192/C192M-07 [32], six of them for the columns batch, and six cylinders for the beams batch. From each batch, two cylinders were tested for splitting strength, and the remaining four were tested for compressive strength. The results of the cylinder tests are illustrated in Table 7.

Table 7. Compressive and Splitting Tensile Strengths of SCC concrete

Batch	Test Type	Number of Specimens	Strength Range (MPa)	Average Strength (MPa)
Columns	Compressive	4	35.5-36.3	36.1
Columns	Splitting	2	3-3.1	3.05
Beams	Compressive	4	34.8-36.1	35.5
Beams	Splitting	2	3.1-3.2	3.1

4. Experimental Program

The overall experimental workflow shows the process of the methodology is illustrated in Figure 4.

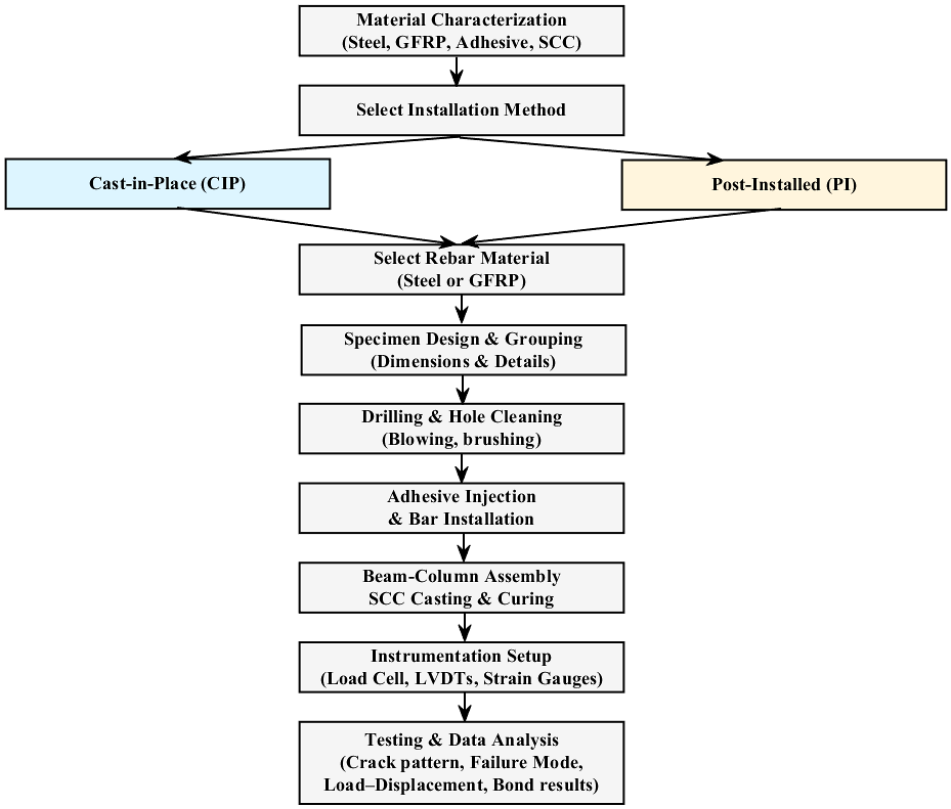

Figure 4. A flowchart illustrating the experimental procedure of the study

4.1. Load Measurement Device

The dimensions of all specimens were identical, but the reinforcing details and installation procedures varied. Figure 5 illustrates the dimensions of a specimen reinforced with 12 mm (GFRP /Steel) post-installed bars. The two identical columns were 1500 mm high, 200 mm wide, and 250 mm long, with four vertical 16 mm Grade 60 rebars, two at each face as longitudinal reinforcement, confined by 10 mm ties spaced at 90 mm intervals as transverse reinforcement. The reinforced concrete rectangular beam was 200 mm in width, 300 mm in depth, and with a length of 1400 mm as a clear span. Four longitudinal reinforcement bars, two at each face with different bar diameters, along with bar materials and installation method, were used in each group set for those beams. The rebar at the connection region was either post-installed or cast-in-place. The beam stirrups were 10 mm in diameter, spaced at 120 mm intervals center to center to be utilized as transverse reinforcement, and a clear concrete cover (40 mm) from all sides of the columns and beam was used. The specimens were divided into three main groups, each group focusing on a specific parameter, to evaluate the effect of bar diameter, bar material, and installation method. Table 8 illustrates the description of each group. The cast-in reference specimen reinforced with steel bars was detailed according to the ACI-318 code [33]. The longitudinal reinforcements on either face of the beam in group 1 consisted of four post-installed GFRP reinforcement bars, two at each face, each specimen reinforced with a different GFRP bar size (12, 16, and 20 mm). The embedment length provided for each specimen was 10db, where db is the diameter of the bar. To evaluate the impact of the installation method, two specimens from group 2 were used. Each specimen's beam was reinforced with GFRP bars, with one using a post-installed method and the other a cast-in method. The bar diameter of the two specimens was kept constant (12 mm). To examine the impact of bar material, each specimen's beam in group 3 was reinforced with either GFRP or steel bars that were post-installed. The bar diameter of the two specimens was kept constant (12 mm).

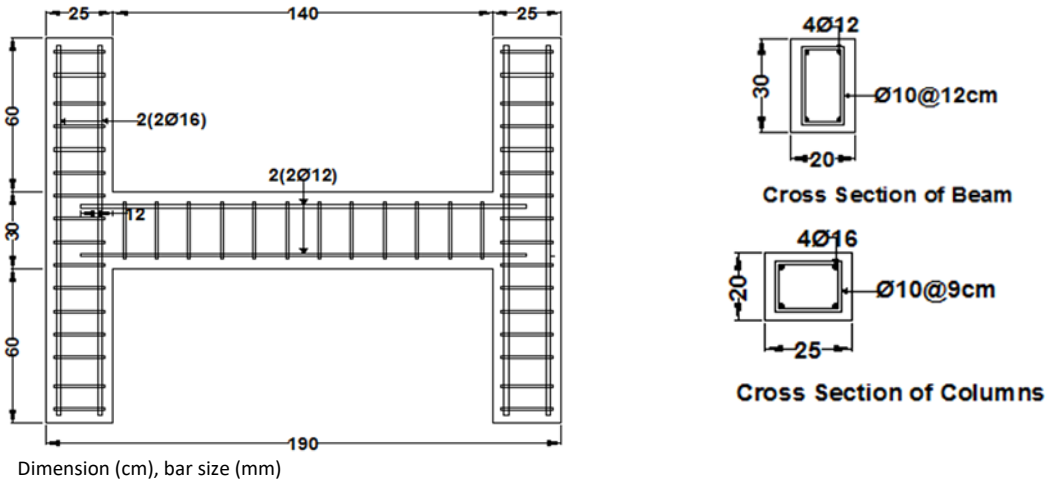

Figure 5. Details of post-installed 12 mm GFRP specimen in group (1)

Table 8. Description of Specimen Groups

Group No.	Description
Group 1	Three Specimens with post-installed GFRP bars, each with a different diameter: 12, 16, and 20 mm
Group 2	Two Specimens with post-installed bars, each with a different bar material: steel or GFRP
Group 3	Two Specimens with GFRP bars, one cast-in and one post-installed

4.2. Construction of the Specimens

The procedure started with preparing the forms and installing the reinforcement for the two columns. The casting of the two columns initiated simultaneously. After casting, lifting hooks were installed, and the concrete surface was smoothed. The formworks were stripped 72 hours after casting, and curing was initiated by covering the concrete surface with a wet burlap for 28 days. The concrete surface regions that will include the beam-column connections interaction were roughened to provide sufficient cohesion. The holes for the beam's post-installed rebars were drilled via a drilling hammer to the intended length; the holes were cleaned via a wire brush and jet air twice. As shown in Figure 6, the adhesives were injected, and the rebars were installed during the set time recommended by the supplier. The stirrups were inserted and distributed along the beam's longitudinal reinforcement. The formwork for the beam was installed, and casting with the same SCC mix was applied, in the same way as for the columns. After 72 hours, the formwork was displaced. The curing process was the same as for the columns.

(a) Post-Installation of Rebar **(b) Stirrup's Placement** **(c) Casting of Beams**

Figure 6. Post-installed specimens

4.3. Testing Method

As shown in Figure 7, the experimental setup included a hydraulic jack centrally positioned to apply a concentrated load at the beam's mid. span. The jack, connected to an automatic hydraulic pump (capacity: 1000 kN), applied load increments of 1 kN. A pressure transducer, along with an in-line dial gauge, was employed to monitor the applied loads. A calibrated LVDT was positioned precisely below the loading point and coupled to a data gathering system that logged at 1 Hz to measure displacement. Crack development was documented and captured at each load phase. To record strain behavior, four 6 mm strain gauges were mounted on the top and bottom reinforcement bars, two at the beam-column connections, as well as two at the mid span. All sensors, which included the LVDT and load cell, have been connected to a TDS-530 data logger to provide for synchronized data collecting during the loading process.

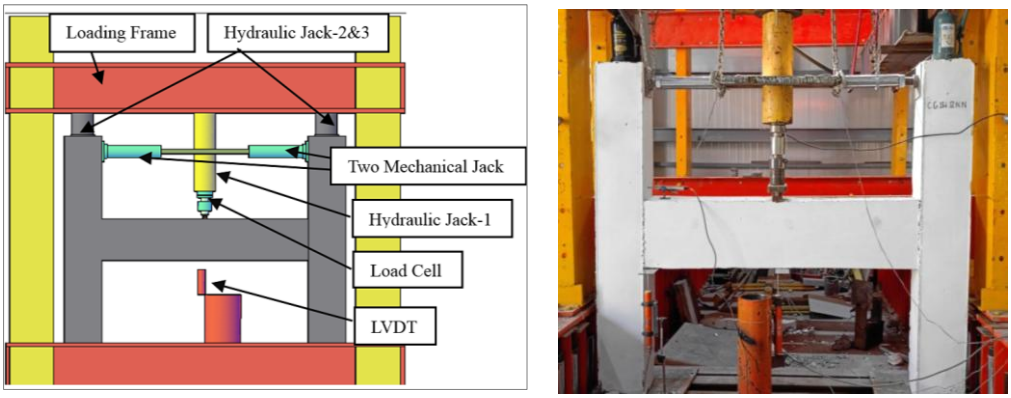

Figure 7. Test setup

5. Results and Discussion

5.1. Crack Pattern and Mode of Failure

The specimens in group 1, as shown in Figures 8 to 10, indicate that the initial crack pattern of the three specimens in this group was similar. For all the specimens in group 1, the first visible cracks appeared at the top tension face of the beam next to the beam-column interface at a load of approximately 30-43 kN, followed by the initiation of vertical cracks at the mid-span of the beam's bottom face at a load of 39-46 kN. As loading progressed, more vertical cracks appeared at midspan, and the first cracks at the interface propagated downward. When the load increased (121-208 kN), a horizontal crack initiated, branched from the initial vertical crack, and extended along the post-installed bars at the columns. Specimens with larger bar diameters (16 and 20 mm) exhibited earlier and more noticeable cracking than the specimen with 12 mm. Earlier cracks are attributed to the system's inability to disperse stresses effectively due to the greater axial stiffness.

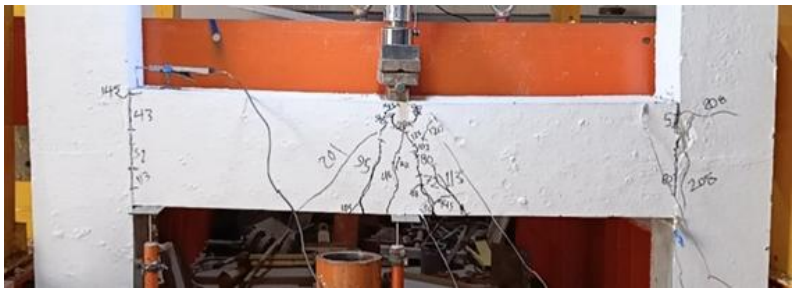

Figure 8. Failure pattern of specimen reinforced with 12 mm post-installed GFRP bars

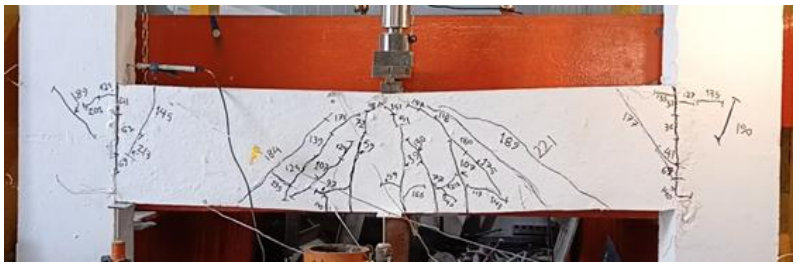

Figure 9. Failure pattern of specimen reinforced with 16 mm post-installed GFRP bars

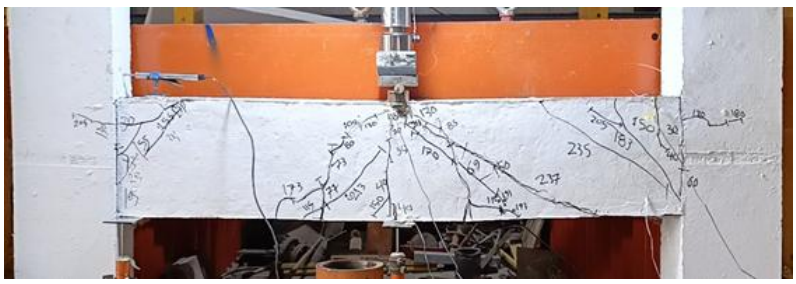

Figure 10. Failure pattern of specimen reinforced with 20 mm post-installed GFRP Bars

Moreover, when the load reached 145 kN, the specimens with larger diameters (16 and 20 mm) experienced flexural cracks at the beam's negative moment regions due to their stiffer response when compared to the 12 mm specimen. At midspan, the 12 mm bar specimen exhibited a pure flexural failure mode, while due to the increased stiffness and stress concentration, the 16 mm and 20 mm bar specimens demonstrated a flexural-shear failure mode. At the connection regions, the specimen reinforced with 12 mm GFRP as post-installed bars failed by concrete splitting combined with bar pull out, whereas specimens with bar sizes of 16 mm and 20 mm failed by concrete cone breakouts.

For group 2, as shown in Figure 11, the first crack of the specimen with post-installed steel bars initiates at the mid-span of the beam's bottom face at 53 kN. As the load increased to 70 kN, the crack widened and extended vertically. Simultaneously, a vertical crack started to appear at the top face of the beam-column interface. As the load increases, additional flexural cracks appear at mid-span, and the interface crack propagates downward. At 160 kN, a horizontal crack initiates at the columns along the embedment length of top post-installed steel bars. At higher loads, concrete splitting cracks formed, and debonding of the steel bars is observed at the connection, as shown in Figure 12. Additionally, the flexural cracks widened at midspan, and a flexural-shear crack was observed near peak load.

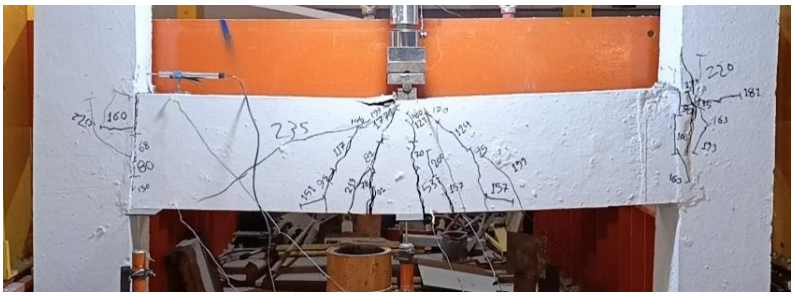

Figure 11. Failure pattern of specimen reinforced with 12 mm post-installed Steel Bars

Figure 12. Pull-Out Failure of PI Steel Bars

In contrast, the GFRP specimen showed its first crack at the top face of the beam-column interface at 43 kN. As the load increased, the interface crack propagated vertically downward, and the first crack at the bottom of the midspan appeared at 46 kN. As loading progressed, multiple flexural cracks showed at midspan. At higher load, the flexural cracks widened, and horizontal cracks initiated along the post-installed GFRP bars combined with slippage of the top GFRP bars, indicating a splitting combined with pull-out mode of failure. The brittle characteristics of GFRP restrict stress redistribution, resulting in rapid expansion of cracks and culminating in abrupt and less ductile failure relative to steel.

For the cast-in specimen in Group 3, as shown in Figure 13, the first visible crack initiated at the bottom face of the midspan of the beam at 43 kN. At 70 kN, the crack extended, and another flexural crack initiated; additionally, at the top face of the interface, a flexural crack initiated. At higher load, flexural-shear cracks were observed at midspan, and a horizontal crack formed along the embedment of the top cast-installed bars. Near the peak load, flexural cracks at the beam's negative moment regions were formed. At peak load, the GFRP rebars ruptured suddenly at mid-span.

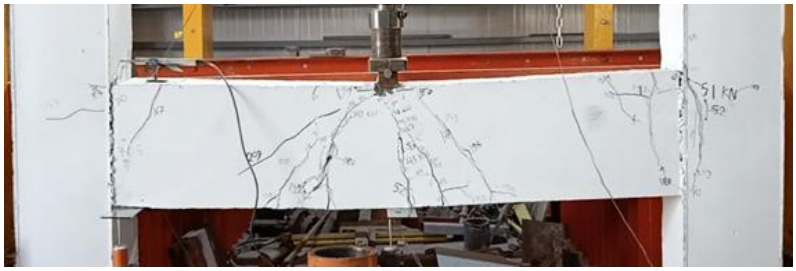

Figure 13. Failure pattern of Specimen reinforced with 12 mm cast-in GFRP bars

In contrast, the post-installed specimen exhibited a sudden drop, indicating that connection failure was the primary mode of failure. First, flexural cracks were initiated and developed in the left end of the beam at the negative moment at the interfaces. Near the ultimate load bond failure (slip) at the connection start, which caused this sudden failure.

5.2. Load-Displacement Behavior

To investigate the load-displacement behavior, the load-deflection curves regarding specimens within various groups were plotted as shown in Figures 14 to 16 to assess initial stiffness, peak load, and ductility. It can be shown from Figure 14 that all specimens in group 1 exhibited elastic behavior in the initial linear portion. Specimens reinforced with 12 mm GFRP rebars showed lower initial stiffness as compared to larger GFRP rebars. This indicates that a larger cross-sectional area increases stiffness. After the first visible crack, the stiffness decreased due to crack propagation.

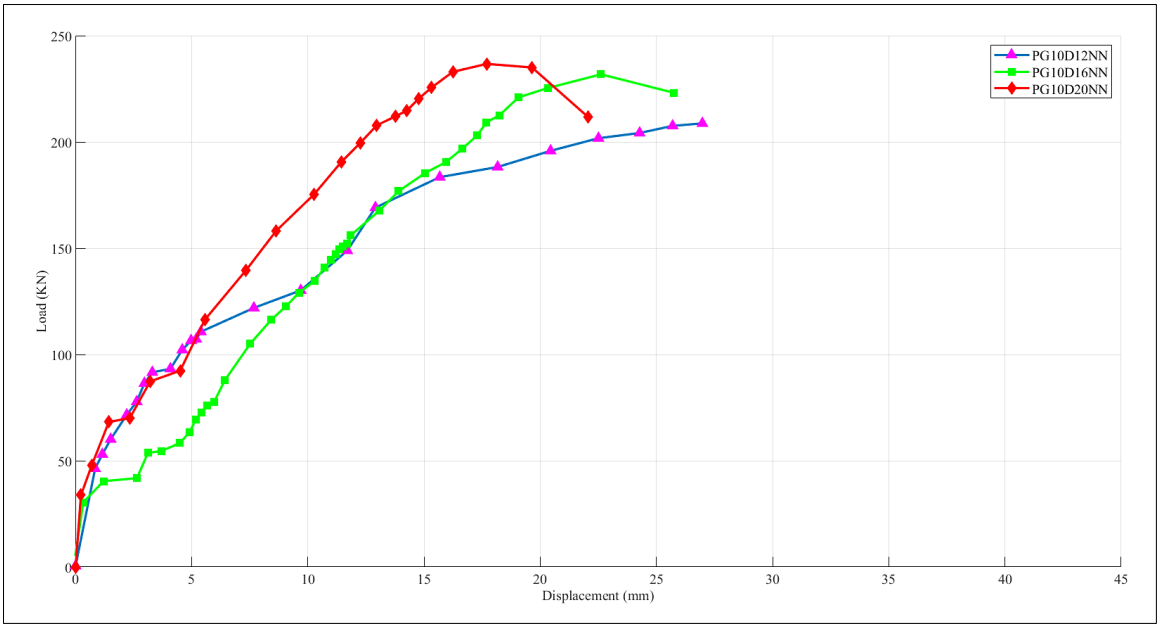

Figure 14. Load-deflection curves of group 1 specimens

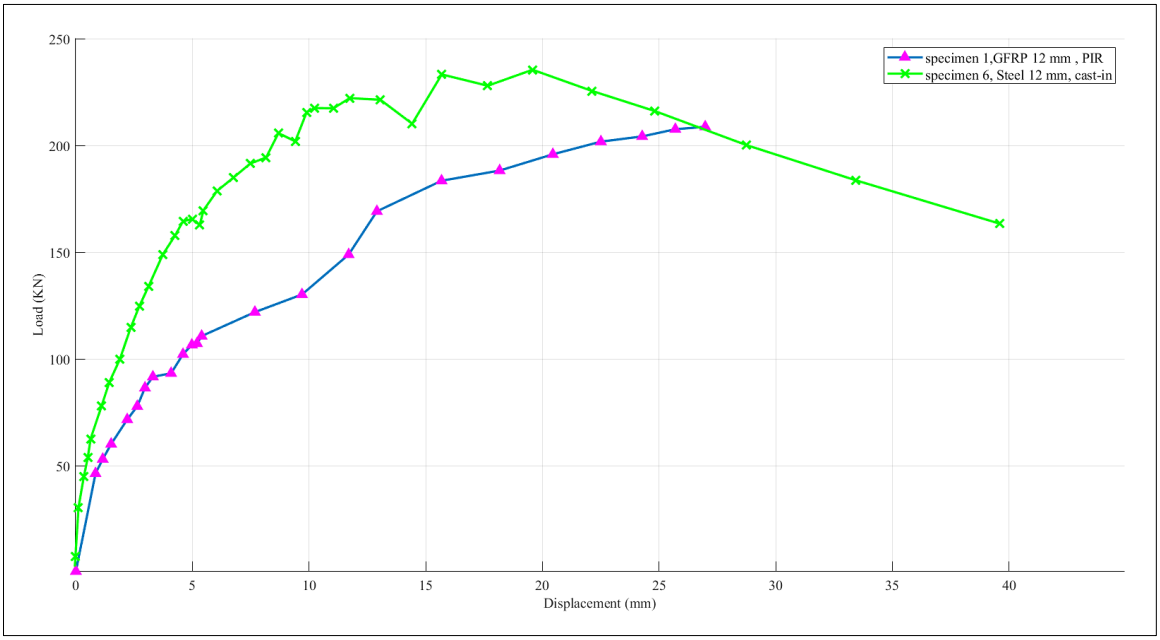

Figure 15. Load-deflection curves of group 2 specimens

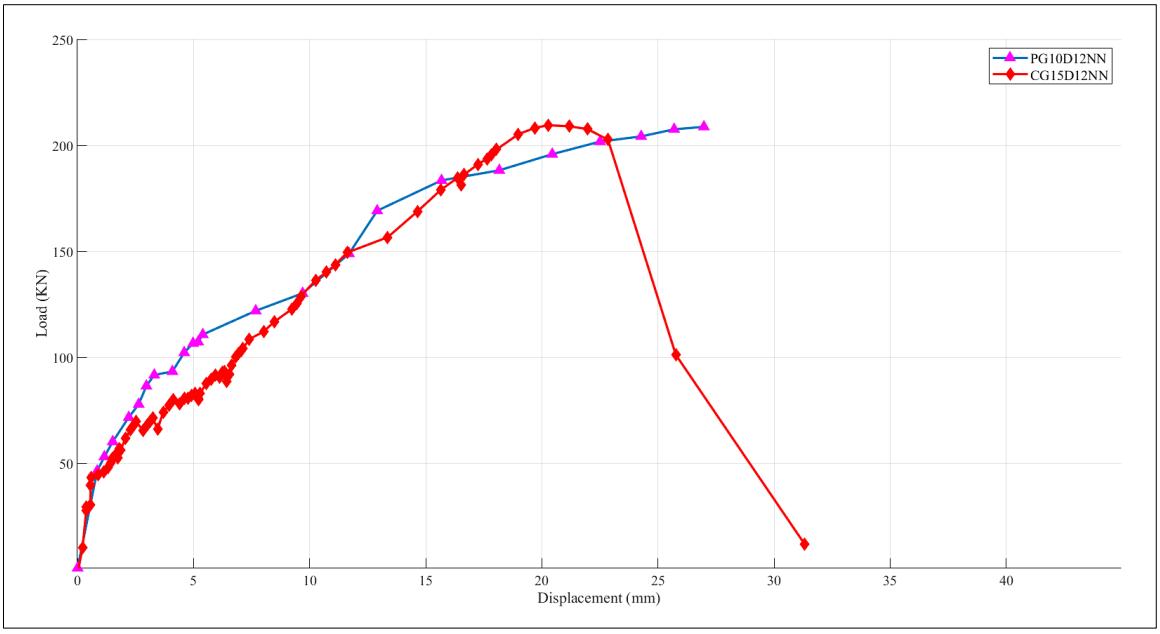

Figure 16. Load-deflection curves of group 3 specimens

For 16 mm and 20 mm specimens, the transition occurred more gradually, contrary to the 12 mm specimen, which exhibited a sharper transition in the load-deflection curve. The peak applied load for each specimen varies with bar diameter. The 20 mm specimen exhibited the highest load of 237.3 kN with a corresponding mid span deflection of 18.71 mm. Peak applied load dropped, and the corresponding deflection increased as the bar diameter decreased. For all specimens, the post-peak exhibited a sudden drop after the peak, indicating a brittle failure. As the bar diameter increased, the drop of the curve was sharper.

Figure 15 illustrates that the two specimens of group 2 demonstrate elastic behavior in the initial elastic portion before the first crack. Specimen reinforced with post-installed steel rebars shows higher initial stiffness as compared to the specimen reinforced with post-installed GFRP rebars, due to the difference in modulus of elasticity of the two materials. After the first visible crack, the stiffness of both specimens decreases significantly. For the steel specimen, stiffness decreases gradually; however, for the GFRP specimen, stiffness decreases rapidly, which is owing to the brittle characteristics of the GFRP material. Additionally, the steel specimen reaches a higher peak load of 235.5 kN as compared to 211.6 kN for the GFRP specimen. On the contrary, the displacement corresponding to the peak load of the steel specimen (19.81 mm) is smaller than that of the GFRP specimen (27.56 mm). The steel specimen shows a more ductile response post-peak load in contrast to the GFRP specimen, which displays a sudden drop at peak load.

For group 3, both specimens, as revealed in Figure 16, show identical linear elastic behavior before the first crack. However, after the first crack, both specimens demonstrate a reduction in stiffness. The cast-in specimen showed a greater reduction in stiffness compared to the post-installed specimen. The adhesive in post-installed specimens provides better bonding for the rebars and helps evenly distribute stresses along the post-installed bars, which increases the specimens' stiffness. Although the two specimens achieved a comparable peak load, the post-installed specimen demonstrated a larger displacement (27.56 mm) than the cast-in specimen (20.69 mm). This indicates that post-installed specimens are more ductile, allowing them to deform without losing their load-bearing capacity.

5.3. Bond Strength and Bond Ratio

Bond strength serves as an indicator for examining the efficiency of the anchorage. In this study, bond strength was calculated using a cracked section analysis approach based on the stress induced on the GFRP rebars at the cracking load [34, 35]. The bond strengths were computed using the following expression:

$$\sigma_f = n \times \left(M_{cr} \times (d - c)\right)/I_{cr} \quad (1)$$

where, n is the modular ratio, M_{cr} is the cracking moment, d is the distance between bars and the compression fiber, d is the depth of the neutral axis, and I_{cr} is the cracked moment of inertia. To enable comparison among specimens with varying parameters. A bond ratio was defined as the ratio of the peak load of a given specimen to that of a reference specimen [12]. A specimen with cast-in steel rebars was considered the reference specimen. The bond ratios for specimens are plotted in Figure 17. Table 9 summarizes the peak loads, corresponding displacements, calculated bond strengths, and bond ratios for all tested specimens.

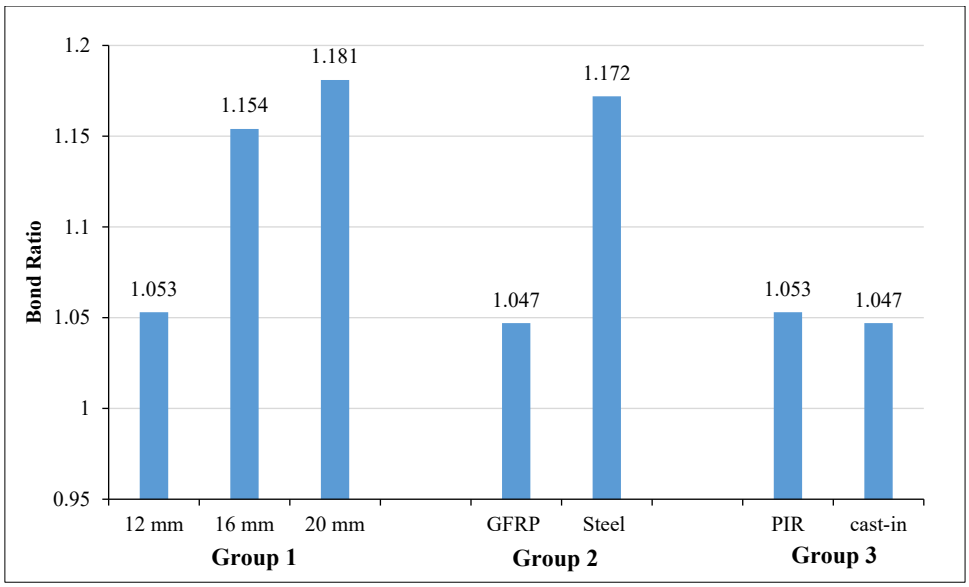

Figure 17. Bond ratios relative to a reference cast-in steel specimen

Table 9. The Peak Loads, Bond Strengths, and Bond Ratios

No.	Bar Diameter (mm)	Bar Material	Installation Method	Maximum Applied Load (kN)	Displacement at Maximum Load (mm)	Bond Strength (MPa)	Bond Ratio
1	12	GFRP	Post-installed	211.6	27.56	714	1.053
2	16	GFRP	Post-installed	232	22.64	446.39	1.154
3	20	GFRP	Post-installed	237.3	18.71	295.9	1.181
4	12	Steel	Post-installed	235.5	19.81	331.63	1.172
5	12	GFRP	Cast-in	210.5	20.69	710	1.047
6	12	Steel	Cast-in	200.9	19.94	282.9	1

For group 1, as the bar diameter increased, the bond strength of the post-installed GFRP bars decreased, even though they attained a higher peak load. This inverse relationship is due to the expanded perimeter surface area, which disseminates bond stresses on GFRP bars more widely. Conversely, the bond ratio increased with larger bar diameter, reflecting the increase in peak load. When the diameter increased from 12 mm to 16 mm, the bond strength decreased by 37.47%, even though the peak load increased by 9.64%. This finding aligns with the previous studies, which demonstrated that an increase in bar size correlates with a reduction in bond strength at a constant embedment depth [36].

The effect of bar material for post-installed bars was demonstrated in group 2. Although the steel specimen achieves an increase of 11.29% in the peak load, the bond strength reduced by 53.5% compared to the GFRP specimens. However, the bond ratio for the steel specimen was slightly higher due to a larger ultimate load value. This behavior can be explained by the differences in material properties. The compatibility of stiffness between the adhesive and the GFRP bars helps on inducing better stress transfer process (i.e., increasing bond strength) as compared to steel bars [5, 18].

Group 3 shows that for specimens with GFRP bars, the bond strength, bond ratio, and peak load of the post-installed specimen and cast-in specimen are similar, with a slight increase in the post-installed specimen's values. For steel specimens, post-installed bars increase bond strength, bond ratio, and peak load by 17.22% compared to cast-in specimens. This indicates the reliable performance of the post-installed specimen and its ability to replicate the performance characteristics of the cast-in specimen effectively. This improvement results from better confinement of the post-installed bars, which provides uniform stress distribution along the bars. These results are consistent with previous studies [37].

5.4. Strain of Longitudinal Reinforcement

Strain data offers insights into flexural behavior, cracking formation, and anchoring performance across various reinforcing materials, bar diameters, and installation techniques. Table 10, and Figure 18 illustrate the recorded strain values at mid span and connection for various bar diameters, installation methods, and materials.

Table 10. Strain Measurements

No.	Bar Diameter (mm)	Bar Material	Strain at the top mid-section	Strain at the bottom mid. section	Strain at the top connection. Section	Strain at the bottom connection Section
1	12	GFRP	0.009244	0.045001	0.008124	0.003091
2	16	GFRP	0.020455	0.046179	0.006703	0.019995
3	20	GFRP	0.017	0.009503	0.007879	0.022562
4	12	Steel	0.001193	0.017763	0.013608	0.004433
5	12	GFRP	0.012183	0.035051	0.025611	0.007261
6	12	Steel	-	0.080007	0.002757	0.002761

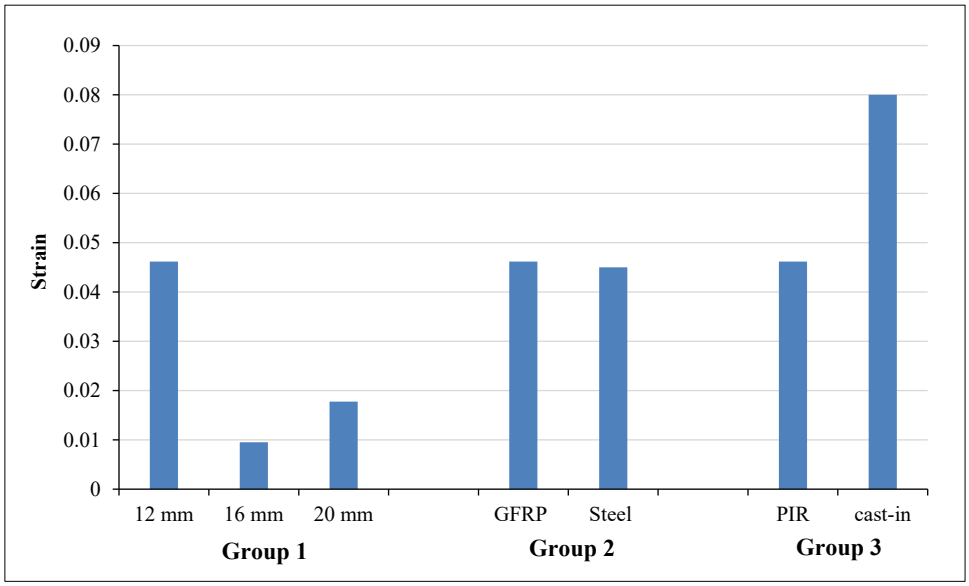

Figure 18. Mid Span Strain at the Beams' Bottom Rebars

At mid span, cast-in steel bars showed the highest strain value, suggesting high flexural performance due to their higher modulus of elasticity. Followed by the post-installed 12 mm GFRP and steel bars, which show strain values of 0.046179 and 0.045, indicating comparable flexural deformation capabilities at peak load. The cast-in GFRP specimen had a slightly lower strain value of 0.035. As the diameter of the GFRP bars increased in the post-installed specimens, the strain values decreased significantly, measuring 0.009503 for the 16 mm specimen and 0.017763 for the 20 mm specimen, owing to increased stiffness.

At the top of the mid span, the related strain followed a similar pattern but with a smaller magnitude. Compression strain was recorded in the 20-mm GFRP bars, indicating a shift in the neutral axis. Cast-in GFRP bars showed the maximum strain value (0.025611) at the beam-column connection, followed by the post-installed 20 mm GFRP bars (0.013608). This indicates an effective transition in stress between the bar and the surrounding concrete along the embedded length.

In contrast, the cast-in steel bars recorded the lowest strain value (0.002757) due to local cracking of the surrounding concrete. The post-installed steel bars, along with post-installed 12 mm and 16 mm GFRP, recorded a comparable strain value of 0.008124, 0.006703, and 0.007879. At the bottom of the connection, strain values of 0.019995 and 0.022562 were recorded for the post-installed 12 mm and 16 mm GFRP bars, respectively, indicating a notable stress transfer. In contrast, the cast-in steel bars exhibited a smaller strain value (0.002761).

6. Conclusions

From the experimental investigation of post-installed (PIR) and cast-in steel and GFRP bars in beam-column connections, the following conclusions can be identified:

- Increasing the diameter of GFRP bars led to earlier initiation of vertical cracks at the beam-column connections, with larger diameters causing flexural cracks at the beam ends and flexural-shear cracking at mid-span. For comparison of bar material, cracks in the GFRP specimen initiate earlier at the interface of the beam-column, whereas in the steel specimen, the first crack is located at the mid-span. Both steel and GFRP specimens experience debonding failure at the connections; however, at the midspan, the steel specimen indicates a shear-flexural crack, whereas the GFRP specimen exhibits pure flexural cracks. Regarding the installation method, the cast-in GFRP

specimen exhibited flexural cracks at the ends of the beam, indicating a stiffer response and better bonding compared to the post-installed specimen. Moreover, the cast-in specimen failed due to the rupture of the GFRP bars, while the post-installed specimen failed mainly due to bar debonding, highlighting the effect of adhesive interfaces on load transfer.

- Regarding load-deflection behavior, increasing the GFRP bar diameter caused an increase in the load capacity and a reduction in the corresponding deflection. The specimen with steel bars achieved a higher load capacity compared to the specimen with GFRP bars. GFRP specimens, however, recorded higher mid-span deflection because of their lower modulus of elasticity. In comparing installation methods, both cast-in and post-installed GFRP specimens recorded a comparable loading capacity. However, the post-installed specimen demonstrated a higher deflection because of minor slip between the adhesive layer and the surrounding concrete.
- Bond performance analysis indicated that increasing the GFRP bar diameter caused a reduction in the bond strength, while the bond ratio and load capacities increased. Although steel bars sustain a higher load capacity, using GFRP bars as an alternative to steel bars results in a higher bonding strength. Post-installed and cast-in GFRP specimens recorded a comparable performance in terms of bond strength, bond ratio, and load capacity.

7. Declarations

7.1. Author Contributions

Conceptualization, B.M.M. and O.A.S.; methodology, S.Y.K.; validation, S.Y.K. and O.A.S.; formal analysis, B.M.M.; investigation, S.Y.K. and O.A.S.; resources, O.A.S.; data curation, B.M.M.; writing—original draft preparation, B.M.M.; writing—review and editing, S.Y.K. and O.A.S.; visualization, S.Y.K. and O.A.S.; supervision, S.Y.K.; project administration, O.A.S.; funding acquisition, B.M.M. and O.A.S. All authors have read and agreed to the published version of the manuscript.

7.2. Data Availability Statement

The data presented in this study are available in the article.

7.3. Funding

The authors received no financial support for the research, authorship, and/or publication of this article.

7.4. Acknowledgments

The authors would like to thank the University of Mosul's Civil Engineering Department Head for their support and the Construction Materials Lab personnel for their help in finishing this study.

7.5. Conflicts of Interest

The authors declare no conflict of interest.

8. References

[1] Khansamrit, K., Intarabut, D., Phiangphimai, C., Hanjitsuwan, S., Sahamitmongkol, R., Phoo-ngernkham, T., Damrongwiriyanupap, N., Petcherdchoo, A., & Chindaprasirt, P. (2025). Evaluation of post-installed adhesive anchors in concrete using hybrid alkali-activated binders. Construction and Building Materials, 471, 140677. doi:10.1016/j.conbuildmat.2025.140677.

[2] Lee, A. Y. F., Su, R. K. L., & Chan, R. W. K. (2019). Structural behaviour of post-installed reinforcement bars in moment connections of wall-slabs. Engineering Structures, 195, 536–550. doi:10.1016/j.engstruct.2019.05.092.

[3] Du, H., Wang, H., Wang, J., Wang, Y., & Yang, F. (2024). Tensile and shear capacity of post-installed chemical adhesive anchors in lightweight concrete. Structures, 61, 106113. doi:10.1016/j.istruc.2024.106113.

[4] Zhao, N. Y., Yang, A., Lin, Y., Jiang, H., & Yi, B. (2025). Experimental Investigation of Adhesive-Related Failures in Post-Installed Rebars under Transverse Pressure. Journal of Building Engineering, 114419. doi:10.1016/j.jobe.2025.114419.

[5] Borkan M. Mutashar, Oday A. Salih, & Suhaib Y. Kasim. (2025). A Review of the Bond Mechanism and Bond Strength of Fiber Reinforced Polymer Rebars to Concrete. Misan Journal of Engineering Sciences, 4(1), 29–45.

[6] Mohammed, A. D., & Asal Salih, O. (2025). An Experimental Study on Reinforced Concrete Beams with GFRP and Ordinary Steel Bars' Flexural Strength Properties. Civil and Environmental Engineering, 28(1), 282–298. doi:10.2478/cee-2025-0022.

[7] Salim, Z. S., Salih, O. A., & Kasim, S. Y. (2022). Investigating the Behavior of Post-Installed Reinforcing Bars Fixed by Chemical Adhesives with Different Concrete Base Compressive Strength. AIP Conference Proceedings, 2660(1). doi:10.1063/5.0107859.

[8] Wang, D., Wu, D., He, S., Zhou, J., & Ouyang, C. (2015). Behavior of post-installed large-diameter anchors in concrete foundations. Construction and Building Materials, 95, 124–132. doi:10.1016/j.conbuildmat.2015.07.129.

[9] Ahmed, K. S., Shahjalal, Md., Siddique, T. A., & Keng, A. K. (2021). Bond strength of post-installed high strength deformed rebar in concrete. Case Studies in Construction Materials, 15, e00581. doi:10.1016/j.cscm.2021.e00581.

[10] Fuchs, W., & Hofmann, J. (2021). Post-installed reinforcing bars – Requirements for their reliable use. Developments in the Built Environment, 5. doi:10.1016/j.dibe.2020.100040.

[11] Cook, R. A., Kunz, J., Fuchs, W., & Konz, R. C. (1998). Behavior and design of single adhesive anchors under tensile load in uncracked concrete. ACI Structural Journal, 95(1), 9–26. doi:10.14359/522.

[12] Hamad, B. S., Al Hammoud, R., & Kunz, J. (2006). Evaluation of bond strength of bonded-in or post-installed reinforcement. ACI Structural Journal, 103(2), 207–218. doi:10.14359/15178.

[13] Spieth, H. A., Ozbolt, J., & Eligehausen, R. (2001). Numerical and experimental analysis of post-installed rebars spliced with cast-in-place rebars. International symposium on connections between steel and concrete, 9-12 September, 2001, Stuttgart, Germany.

[14] Mahadik, V., Sharma, A., & Hofmann, J. (2020). Re-evaluation of existing tests on RC connections using post-installed reinforcing bars. Engineering Structures, 209. doi:10.1016/j.engstruct.2019.109970.

[15] BS EN 1992-1-1:2004+A1:2014. Eurocode 2: Design of concrete structures - General rules and rules for buildings. British Standard Institution (BSI), London, United Kingdom.

[16] EN 1992-4. (2018). Eurocode 2–Design of Concrete Structures–Part 4: Design of Fastenings for Use in Concrete. European Commitiee for Standardization (CEN), Brussels, Belgium.

[17] Mahrenholtz, C., Eligehausen, R., & Reinhardt, H. W. (2015). Design of post-installed reinforcing bars as end anchorage or as bonded anchor. Engineering Structures, 100, 645–655. doi:10.1016/j.engstruct.2015.06.028.

[18] Agarwal, J. (2023). Bond behavior of post-installed Glass fiber reinforced polymer (GFRP) rebars. Master Thesis, Purdue University, West Lafayette, Indiana.

[19] Chea, L., Doung, P., Dimanche, S., & Leelataviwat, S. (2025). Evaluation of bond strength and failure modes of post-installed bundled reinforcing bars embedded in concrete structure. Construction and Building Materials, 500. doi:10.1016/j.conbuildmat.2025.144232.

[20] Mizan, M. H., Hayakawa, R., & Matsumoto, K. (2025). Effects of combined deterioration of steel corrosion and freeze-thaw cycles on the pull-out behavior of deformed bars in concrete. Construction and Building Materials, 505. doi:10.1016/j.conbuildmat.2025.144758.

[21] Mishra, V., & Sadhu, A. (2023). Towards the effect of climate change in structural loads of urban infrastructure: A review. Sustainable Cities and Society, 89. doi:10.1016/j.scs.2022.104352.

[22] Xie, F., Tian, W., Li, S., Diez, P., Zlotnik, S., & Gonzalez, A. G. (2025). Experimental Study on the Structural Performance of Glass-Fiber-Reinforced Concrete Slabs Reinforced with Glass-Fiber-Reinforced Polymer (GFRP) Bars: A Sustainable Alternative to Steel in Challenging Environments. Polymers, 17(8). doi:10.3390/polym17081068.

[23] Mahrenholtz, P. (2013). Experimental performance and recommendations for qualification of post-installed anchors for seismic applications. PhD Thesis, Institut für Werkstoffe im Bauwesen der Universität Stuttgart, Stuttgart, Germany.

[24] ACI 440.3R. (2004). Guide Test Methods for Fiber-Reinforced Polymers (FRPs) for Reinforcing or Strengthening Concrete Structures. American Concrete Institute (ACI), Farmington Hills, United States.

[25] ASTM A615/A615M-01b. (2017). Standard Specification for Deformed and Plain Billet-Steel Bars for Concrete Reinforcement. ASTM International, Pennsylvania, United States. doi:10.1520/A0615_A0615M-01B.

[26] ASTM C150/C150M-24. (2024). Standard Specification for Portland Cement. ASTM International, Pennsylvania, United States. doi:10.1520/C0150_C0150M-24 .

[27] ASTM C136/C136M-14. (2020). Standard Test Method for Sieve Analysis of Fine and Coarse Aggregates. ASTM International, Pennsylvania, United States. doi:10.1520/C0136_C0136M-14 .

[28] Mardani-Aghabaglou, A., Tuyan, M., Yilmaz, G., Ariöz, Ö., & Ramyar, K. (2013). Effect of different types of superplasticizer on fresh, rheological and strength properties of self-consolidating concrete. Construction and Building Materials, 47, 1020–1025. doi:10.1016/j.conbuildmat.2013.05.105.

[29] DCP. (2024). Hyperplast PC200: Technical Data Sheet. Don Construction Products (DCP), Haverhill, United Kingdom.

[30] Sika Services AG. (2024). Sika AnchorFix-3030: Product Data Sheet (Version 02.03). Sika Services AG, Baar, Switzerland.

[31] EFNARC. (2002). Specification and Guidelines for Self-Compacting Concrete. European Federation of National Associations (EFNARC), Farnham, United kingdom.

[32] ASTM C192/C192M-07. (2012). Standard Practice for Making and Curing Concrete Test Specimens in the Laboratory. ASTM International, Pennsylvania, United States. doi:10.1520/C0192_C0192M-07 .

[33] ACI 318-19. (2019). Building Code Requirements for Structural Concrete and Commentary. American Concrete Institute (ACI), Farmington Hills, United States. doi:10.14359/51716937.

[34] Charney, F. A., Pal, K., & Silva, J. (2013). Recommended procedures for development and splicing of post-installed bonded reinforcing bars in concrete structures. ACI Structural Journal, 110(3), 437–446. doi:10.14359/51685601.

[35] Bajwa, M. S. (2018). Bond behavior of post-installed GFRP bars in structural connections. Master Thesis, University of Minnesota, Minneapolis, United States.

[36] Yan, F., Lin, Z., & Yang, M. (2016). Bond mechanism and bond strength of GFRP bars to concrete: A review. Composites Part B: Engineering, 98, 56–69. doi:10.1016/j.compositesb.2016.04.068.

[37] Tayeh, B. A., EL dada, Z. M., Shihada, S., & Yusuf, M. O. (2019). Pull-out behavior of post installed rebar connections using chemical adhesives and cement based binders. Journal of King Saud University - Engineering Sciences, 31(4), 332–339. doi:10.1016/j.jksues.2017.11.005.